

● *Original Contribution*

A QUANTITATIVE COMPARISON OF MODULUS IMAGES OBTAINED USING NANOINDENTATION WITH STRAIN ELASTOGRAMS

S. SRINIVASAN,* T. KROUSKOP^{†‡} and J. OPHIR[†]

*Siemens Ultrasound Division, Siemens Medical Solutions, Mountain View, CA, USA; [†]Department of Radiology, Ultrasonics Laboratory, The University of Texas Medical School, Houston, TX, USA; and [‡]Department of Physician Medicine and Rehabilitation, Baylor College of Medicine, Houston, TX, USA

(Received 25 November 2003; revised 22 April 2004; in final form 6 May 2004)

Abstract—Tissue stiffness is generally known to be associated with pathologic changes. Ultrasound (US) elastography, on the other hand, is capable of imaging tissue strain, which may or may not be well-correlated with tissue stiffness. Hence, a quantitative comparison between the elastographic tissue strain images and the corresponding tissue modulus images needed to be performed to evaluate the usefulness of elastography in imaging tissue stiffness properties. Simulations were performed to demonstrate and quantify the similarities between modulus images and strain elastograms. This was followed by comparing nanoindenter-based modulus images with strain elastograms of thin slices of tissue-mimicking phantoms. Finally, some beef slices, canine prostates, ovine kidneys and breast cancers grown in mice were used to demonstrate the qualitative correspondence between modulus images and strain elastograms. The simulations and the experiments indicated that it is feasible to perform quantitative comparisons between strain images (using elastography) and modulus images on certain tissue structures and geometries. A good quantitative correspondence (correlation values of greater than 0.8) between structures in the modulus and strain images could be obtained at scales equal to or larger than $20 Q\lambda$ (where Q is the quality factor defined as the ratio of the center frequency over the band width and λ is the wavelength of the US system) modulus contrasts larger than 5, applied strains between 0.5% and 3% and window lengths for computing strain elastograms between $3 Q\lambda$ and $5 Q\lambda$. The gelatin-phantom experiments showed lower values of correlation (values around 0.5) than with theory and simulations. The decrease in correlation was attributed to the presence of measurement noise in both strain elastography and modulus imaging, an increase of dimensionality of the problem (from 2-D to 3-D), local anisotropy, heterogeneity and nonstationarity. Experiments on real tissue slices showed further decrease in the correlation to around 0.3, possibly due to additional confounding factors such as time-dependent mechanical properties and geometrical distortions in the tissue during imaging. The work presented in this paper demonstrates that there is an intrinsic relationship between strain elastograms and the actual distribution of soft tissue elastic moduli, and bodes well for continued work in the area of elastography. (E-mail: jonathan.ophir@uth.tmc.edu) © 2004 World Federation for Ultrasound in Medicine & Biology.

Key Words: Nanoindentation, Indentation, Modulus imaging, Modulus measurement, Young's modulus, Ultrasound, Elastography, Correlation coefficient, SNR, CNR, Resolution, Scale.

INTRODUCTION

Elastography has been well established in the literature as a strain imaging technique for soft tissues (Ophir et al. 1991, 1999; Emelianov et al. 1995; Pesavento et al. 1999). Conventional techniques in ultrasound (US) elastography estimate strain as the gradient of the displacement estimates obtained through cross-correlation of the pre- and postcompression radiofrequency (RF) A-lines.

Typical applications of elastography include differentiating cancers from noncancers in the breast (Garra et al. 1997; Hall et al. 2001), tumor identification in the prostate (Hiltawski et al. 2001; Lorenz et al. 1999) and in monitoring high-intensity focused US (HIFU) lesions (Righetti et al. 1999; Souchon et al. 2003). Elastography has also been used to image the myocardium (Konofagou et al. 2002), to study renal pathology (Emelianov et al. 1995), to monitor thermal changes (Varghese et al. 2002) and to obtain the structural properties of different normal tissue types (Kallel et al. 1998). Yet, the quantitative aspect of elastography has not been established because the tissue strain is not a fundamental tissue property and

Address correspondence to: Jonathan Ophir, Department of Radiology, Ultrasonics Laboratory, The University of Texas Medical School, 6431 Fannin St., MSB 2.100, Houston, TX 77030 USA. E-mail: jonathan.ophir@uth.tmc.edu

it depends on the tissue modulus and other factors, such as the boundary conditions, the tissue connectivity and the geometry. Therefore, a comparison of the strain elastograms with the modulus images would facilitate the usefulness of US elastography in portraying and quantifying tissue properties such as the tissue modulus.

Modulus imaging is feasible in *in vitro* and *ex vivo* conditions although, in *in vivo* applications, noninvasive direct modulus imaging is difficult. Current *in vivo* modulus imaging techniques are predominantly based on pressure maps that are capable of providing relative modulus measurements of large inclusions close to the tissue surface (Wellman and Howe 1997; Howe 1995; Sarvazyan 1998). Acoustic radiation force imaging is an emerging technology that shows the potential for measuring localized tissue displacements and force, which, in turn, could be used to obtain the localized tissue modulus (Nightingale et al. 2002; Trahey et al. 2002). Other *in vivo* modulus imaging methods involve reconstructing the modulus images from estimates of strain or displacement images (Skovoroda et al. 1995; Kallel and Bertrand 1996; Sumi et al. 1995; Doyley 1999). These methods utilize inverse problem approaches and suffer from several limitations, such as nonuniqueness of the solution, unstable solutions, noise and artefacts in the resulting modulus images and poor spatial resolution of the modulus images. Moreover, studies comparing the reconstructed modulus images with mechanically measured modulus images have not yet been reported.

The characterization of the mechanical properties of tissue is described well in the literature (Krouskop et al. 1998; Duck 1990; Fung 1993; Gao et al. 1996; Sarvazyan et al. 1995; Chen et al. 1996). Yet, imaging the modulus using mechanical measurements is not common, due to restrictions in the precision of the instruments in terms of the spatial resolution (typically greater than 2 mm) as well as the thickness of the samples measured (typically greater than a few mm). For accurate modulus measurements, thin tissue slices are preferred over thick slices because thin slices are likely to be more homogeneous in the tissue depth than thick samples. For similar reasons, high spatial resolutions are preferred. With the use of new technologies, such as nanoindentation (Oliver and Pharr 1992) and atomic force microscopy (Binnig et al. 1986), it could be feasible to image the modulus of thin samples of soft tissues (that are likely to be homogeneous in the entire thickness) at high spatial resolution. Microindentation, where the precision of the indent depths are a few micrometers, has been used to measure the modulus of biologic tissues such as arteries (Anderson et al. 2001) and nanoindentation (the precision of the indent depths are a few nanometers) has been used for bone porosity assessment (Rho et al. 2002).

The principle of nanoindentation is briefly explained as follows. A high-resolution actuator forces an indenter (a punch of a given shape; for example, a cylinder, pyramid or sphere) into the test surface and a high-resolution sensor continuously measures the resulting penetration. Data are acquired during the unloading phase to obtain the elastic properties because plastic deformations could occur during loading and, as a consequence, the measurements of the elastic properties could be corrupted by the plastic changes. The use of short time periods (*i.e.*, rapid loading) and small strains during loading minimizes the effects of hysteresis due to the viscoelastic behavior of the tissue, resulting in nearly identical load-displacement curves during loading and unloading. From the load vs. displacement curve during unloading, the elastic modulus of the sample is estimated. More details on the nanoindenter and can be found in Srinivasan et al. (2004).

Srinivasan et al. (2004) have shown the feasibility of imaging the modulus of soft tissues using nanoindentation and also have provided preliminary results on an experimental comparison of modulus images with strain elastograms obtained using US. In this work, we provide a simulation and experimental framework for comparing the modulus images with strain elastograms and also provide bounds on the performance of nanoindentation in imaging soft-tissue modulus. The following section details the simulation and experimental framework for comparing modulus images with strain images. The results and discussion of the results are provided subsequently.

FRAMEWORK FOR COMPARING MODULUS IMAGES WITH STRAIN ELASTOGRAMS

Some of the factors that affect the correspondence between the modulus and strain include the tissue mechanical properties, such as the Young's modulus, the Poisson's ratio and other controlling factors, such as the geometry of the tissue structures, the modulus distribution of the tissue structures, the scale of the structures, the modulus contrast between tissue structures, the applied strain, the connectivity among the tissue structures and the boundary conditions. To compare the modulus images with the strain elastograms, an exhaustive study of all possible controlling factors is not feasible. We, therefore, restricted the scope of this work to a simple geometry that consists of a stiff cylindrical inclusion inside a homogeneous background. This geometry was chosen as a gross (first order) approximation of the cross-sections of hard cancerous and noncancerous inclusions inside soft tissue (Garra et al. 1997). Cylindrical inclusions were preferred over spherical inclusions to provide plane-strain conditions, as well as to provide

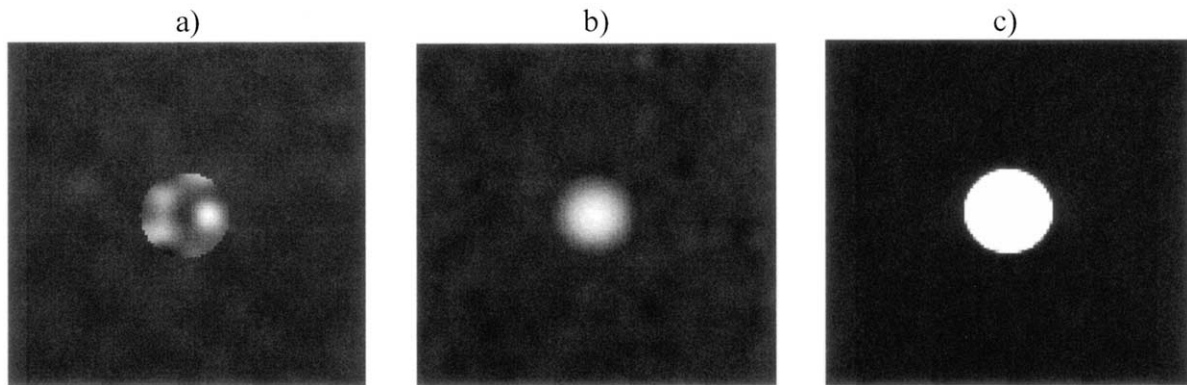


Fig. 1. Simulated modulus image of (a) a normal random distribution in the inclusion and background, (b) a Gaussian modulus profile in the inclusion and a random distribution in the background, and (c) a constant modulus in the inclusion and in the background.

sample homogeneity (in depth) during modulus imaging. 2-D simulations, phantom experiments and experiments on real tissue samples were used to compare the modulus images with strain elastograms.

Simulations

2-D simulations in FEMLAB® (Comsol Inc., Burlington, MA) were performed to simulate circular inclusions in a background. The background was simulated as a $40 \times 40 \text{ mm}^2$ cross-section with slippery boundary conditions. Three types of modulus distributions were used: these were 1. a normal random distribution for the background as well as the inclusion, 2. a Gaussian modulus profile for the inclusion and a normal random distribution for the background, and 3. a constant modulus distribution in the background as well as in the inclusion, as shown in Fig. 1. These distributions were chosen to simulate the types of nonhomogeneities that are likely to occur in the elastograms of cancer samples (Garra *et al.* 1997; Krouskop *et al.* 1998).

Because FEMLAB® allowed the use of functions to set the modulus distribution, we were able to implement random modulus distributions for the background, as well as the target. The scale of the nonhomogeneities was changed from 0.5 mm to 2 mm and the modulus image was obtained for each scale as follows. A 2-D random distribution of moduli was chosen with a grid size that was the ratio of the target size to the scale. The pixel size in FEMLAB® was chosen to be much smaller than the size of the scale and a nearest-neighbor interpolation of the modulus distribution was done to provide the modulus at every pixel in the image. Finally, a blurring function was used at the FEMLAB® grid edges, to avoid setting singularities in the numerical method. The diameters of the inclusions were varied between 2.5 mm and 20 mm. Based on the available literature on the modulus

measurements of certain cancerous and noncancerous lesions in the breast and in the prostate (Krouskop *et al.* 1998), the modulus contrast between the inclusion and the background was set between 1.5 and 10. The applied strain was set between 0.25% and 4% (typical experimental range in elastography). A total of 50 realizations (with differing random-number seed values for the modulus distributions) were used for each case to compute the statistics. The RF A-lines were generated using the procedure described in detail in Srinivasan *et al.* (2003). A 5-MHz, 60% fractional bandwidth and 1-mm beam width transducer was used in the simulations to mimic the experimental conditions (at the focus).

A hybrid adaptive strain estimation procedure was used to obtain the elastograms. In the first step, a two-stage adaptive strain estimation algorithm with lateral motion compensation (Srinivasan *et al.* 2002b) was used to obtain the displacement and strain estimates. In the next step, a true-adaptive strain estimation algorithm (Alam *et al.* 1998) was used to obtain the strain. The first stage was done to initialize the search for true-adaptive strain estimation and, thereby, to improve the speed of the algorithm. The second stage was used to improve the contrast-to-noise ratio (CNR) of the strain estimates (Srinivasan 2003).

The comparison between the modulus images and strain elastograms was done predominantly using the first and second order statistics, as opposed to using higher order statistics. This was because of the relatively smaller sensitivity of these statistics to image noise, unlike higher order statistics. The first order statistics used were the mean, the SD and the contrast (defined as the ratio of the mean strain in the inclusion over the mean strain in the background or, alternatively, as the ratio of the mean modulus in the background to the mean modulus in the inclusion). The second order statistics, such as

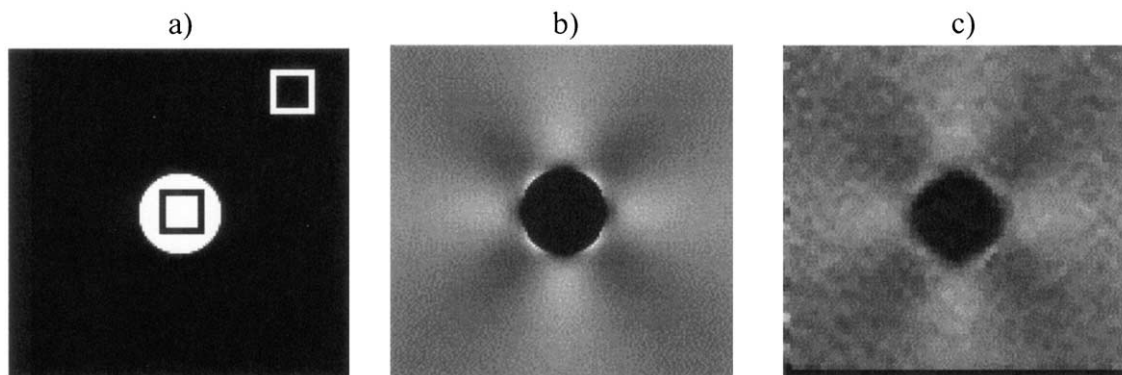


Fig. 2. (a) Simulated modulus image, (b) numerical strain image, and (c) elastogram of a circular inclusion 10 times stiffer than the background. A linear range of 0 to 2% was used for the displays in (b) and (c). A linear range from 1 to 20 kPa was used for the display in (a). The square boxes in (a) indicate the regions from which the statistics were computed.

the cross-correlation, size and shape were chosen. The first order statistics were used to corroborate prior findings on the contrast-transfer efficiency (Kallel et al. 1996) from modulus to strain, and were computed by choosing rectangular strips of pixels from the background and the inclusion of the strain image. In the background, a region that was at least one diameter away from the inclusion was selected and, in the inclusion, a region close to the center of the inclusion was selected, as indicated by the square boxes in Fig. 2. Figure 2b shows the numerical strain image and Fig. 2c shows the strain elastogram corresponding to the modulus image shown in Fig. 2a. It can be seen that the strain elastogram is a noisy representation of the numerical strain image.

Cross-correlation was used to quantify the degree of structural correspondence between the inverted modulus and the strain images. The choice of circular targets permitted the use of autocorrelation to compute the sizes and shapes of the targets. The distance between the minima of the autocorrelation function (with the image means subtracted) in the axial and lateral directions corresponded to twice the size of the inclusion in the axial and lateral directions. The inclusion size was computed as the mean of the sizes in the axial and lateral directions. A parabolic interpolation was done around the minima to obtain subpixel measurements of the sizes. Shape was quantified crudely as the ratio of the lateral to the axial sizes. Again, such a crude shape measure might be adequate for circular cross-sections, and is not applicable in general. Cross-correlation was performed by choosing a square region-of-interest (ROI) around the inclusion, so that the area of the inclusion was almost the same as the area of the background. This is because the contribution to the correlation is negligible if the inclusion size is very small compared with the ROI and *vice versa*. The correlation coefficient ρ_{me} (after subtracting the means from

the images) was computed between the inverted modulus image and the elastogram. Specifically, the equation for ρ_{me} is given by:

$$\rho_{me} = \frac{C_{xy}}{\sqrt{C_{xx}C_{yy}}} = \frac{E[(x - \mu_x)(y - \mu_y)]}{\sqrt{E[(x - \mu_x)(x - \mu_x)]E[(y - \mu_y)(y - \mu_y)]}} \quad (1)$$

where x and y are, respectively, the pixel values of the inverted modulus image and the strain elastogram and μ_x and μ_y are the mean values of the inverted modulus image and the strain elastogram.

The image size of the elastogram was matched with that of the modulus images by performing a bilinear interpolation of the elastogram. Note that the image quality features, such as the signal-to-noise ratio (SNR), CNR and the spatial resolution (Srinivasan et al. 2003), affect the correlation between the inverted modulus images and the strain elastograms.

Phantom experiments

An experimental comparison of the modulus images with strain elastograms was made using tissue-mimicking phantoms made of gelatin-agar-water mixtures. Cylindrical inclusions were made using reinforced sponge material. The phantoms were prepared by inserting 100 pores-per-inch (4 pores-per-mm) open-celled sponge cylinders (made of polyester material) inside the gelatin-agar-water mixture (5% by weight gelatin and 2% by weight agar), squeezing out the bubbles inside the sponge, allowing the sponge to retrieve its original size, followed by cooling the mixture for several h (Kallel et

al. 2001). The porosity was chosen so that the pore size allowed the gelatin to penetrate the sponge and also so that the pore size was much smaller than the size of the sponge sample used. The phantoms were imaged with a 5-MHz, 60% fractional band width 128-element HDI-1000 array scanner (ATL-Philips, Bothell, WA) at three planes orthogonal to the long axis of the cylinder. At each imaging plane, five elastograms were obtained and were averaged. A precompression of 1% was used and elastograms were obtained at several strains ranging from 0.25% to 5%.

Thin slices in the imaging planes (2- to 3-mm thick) were cut and tested using a nanoindenter (Testworks Inc, Nashville, TN) that had a 2-mm diameter cylindrical punch. The spacing of the indentations was such that at least five indentations were present within the width of the sample and a total of 16×16 indentations were performed on each sample. A strain-rate of 1% per s up to a maximum strain of 6% was applied. The modulus at a strain of 2% was compared with the strain elastograms obtained at 1% strain (because a precompression of 1% was used for the elastograms). The period of testing for each sample was approximately 5 h. The samples were preserved in silicone oil before testing and were immersed in water while performing the indentation tests. Note that the elastograms were imaged in a direction orthogonal to the modulus images. Yet, a good similarity was found between the modulus images and the elastograms, as detailed in the Results section.

Several phantoms, each containing a sponge cylinder that ranged between 2.5 mm to 20 mm, were prepared. Five cylindrical sponge samples for each size were used. For each phantom, elastograms and modulus images were obtained at three planes orthogonal to the cylindrical axis, resulting in 15 independent realizations. For a 20-mm sponge size, the modulus contrast ratio between the inclusion and the background was changed from 1.5 to 10. This was done by changing the sponge material (from very soft sponges to hard sponges), while retaining the same concentration of the gelatin-agar mixture; 5 cylindrical sponge samples were used at each contrast, totaling 15 realizations. Finally, complex phantoms containing two 5-mm diameter hard sponge cylinders inside a 20-mm diameter soft sponge cylinder at differing locations were prepared. Eight realizations were used for this model to obtain the statistics.

The spatial resolution of the elastograms was matched with those corresponding to the modulus images. The nanoindenter characterization experiments produced a spatial resolution of 2 mm for the modulus images for unconnected samples and 3 mm for connected samples (Srinivasan *et al.* 2004). A 2-mm window at 80% overlap was used to compute the elastograms. This corresponded to an axial resolution of 2.4 mm (Sriniva-

Table 1. Parameters used during nanoindentation of the *ex-vivo* slices

Tissue type	<i>n</i> of samples	Sample dimensions	<i>n</i> of indentations	Indentation spacing (axial and lateral) (mm)
Beef muscle	3	$30 \times 20 \text{ mm}^2$	150	2
Ovine kidney	4	$52.8 \times 28.6 \text{ mm}^2$	312	2.2
Canine prostate	2	$15 \times 10 \text{ mm}^2$	260	0.75
Colon cancer	4	$24 \times 13 \text{ mm}^2$	312	1

san *et al.* 2003). The pixelation of the modulus and strain images (more than 250 pixels per image) was sufficient to ensure an unbiased correlation. The modulus images were interpolated using a linear interpolation scheme to produce the same number of pixels as the elastograms. Note that, in simulations, the elastograms were interpolated to the size of modulus images because the modulus images were produced with small grid spacings (< 0.2 mm) to produce accurate displacement fields (during the numerical simulation of the displacement fields using FEMLAB®).

Tissue experiments

Tissue samples such as beef-muscle, ovine kidneys, canine prostates and human colon cancers grown in mice were used for the comparison. Table 1 summarizes the experimental parameters used for nanoindentation. The tissue slices were approximately 3-mm thick. The beef slices were obtained commercially (Jordan's Foods, Houston, ME). The ovine kidneys were obtained from a local abattoir. The canine prostates and the HT-29 human colon carcinoma samples were obtained from our institution. The tissue samples were disposed of in accordance with our institution's biologic waste disposal protocol.

RESULTS

Simulation and phantom experiment results

The effect of the signal-processing parameters, such as the window length (W) and the window shift (ΔW), on the comparison between modulus and strain images was first studied. This was done because the elastographic image quality (typically quantified through factors such as SNR, CNR and the spatial resolution) depends on W and ΔW (Varghese and Ophir 1997; Srinivasan *et al.* 2003). Srinivasan *et al.* (2003) demonstrated a nonlinear trade-off between SNR and spatial resolution. Figure 3a shows the normalized first order statistics (the strain contrast and the SD of the strain in the inclusion) and Fig. 3b shows the normalized second order statistics (the

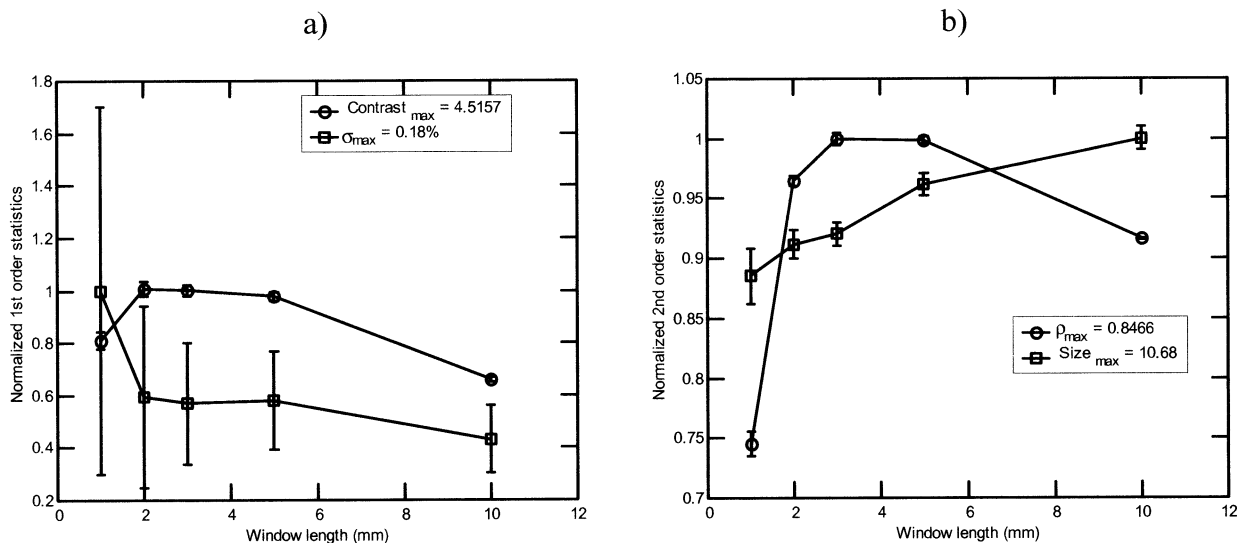


Fig. 3. (a) First order statistics and (b) second order statistics plotted as a function of the window size for a 10-mm diameter homogeneous circular inclusion in a homogeneous background. The inclusion was 10 times stiffer than the background and a strain of 1% was applied. The simulated elastograms were computed at an overlap of 80% of the window size.

inclusion size on the strain image and ρ_{me}) plotted as a function of W . The maximum of the mean values for each curve (*i.e.*, SD, contrast, etc.) was used as the normalization factor, as indicated by the legends in Fig. 3. The use of the mean values instead of the absolute maximum values was preferred to scale the curves because the absolute maximum values could be outliers. Henceforth, the normalized curves were computed by the procedure mentioned above. The value of ρ_{me} shows a convex-shaped behavior with respect to the window length (Fig. 3b). This initial improvement in the value of ρ_{me} with the window length (Fig. 3b) is due to improvement of the SNR and CNR. However, for large window lengths (greater than half the inclusion size), a decrease of the value of ρ_{me} (Fig. 3b) occurs, due to a loss of contrast (Fig. 3a). Similarly, the use of very small window lengths results in high noise in the elastograms (Fig. 3a) and, hence, a poor correspondence with the modulus images (*i.e.*, low values of ρ_{me}). There is a loss of spatial resolution in the elastograms and, hence, inaccurate size measurements (Fig. 3b) for large window sizes accompanied with a loss of contrast (Fig. 3a). Hence, intermediate window sizes that provide an adequate number of independent samples in the target-of-interest are preferred. In general, values of W in the range of $3 Q\lambda$ and $5 Q\lambda$ (where Q is the quality factor defined as the ratio of the center frequency over the band width and λ is the wavelength of the US system) were found to provide a good compromise between axial resolution and the contrast (or the value of ρ_{me}). A 2-mm window size was, therefore, preferred.

Figure 4 shows the first order and second order statistics plotted as a function of the window overlap. It can be seen that the correlation coefficient improves nearly asymptotically with the window overlap (Fig. 4b). To demonstrate an asymptotic behavior, ANOVA tests were used. The values of ρ_{me} for overlaps larger than 50% were not found to be different from each other, but were found to be significantly higher than those obtained at 0% and 20% overlap (p values < 0.05 using ANOVA). The inclusion sizes (Fig. 4b) as well as the contrast and the SD (Fig. 4a) also showed a convergence to the true values for large window overlaps. This indicates that large overlaps ($> 75\%$) are preferred, to provide an adequate sampling of the strain image. A 2-mm window at 80% overlap was henceforth used for computing the elastograms.

Figure 5a shows the modulus image of a 15×20 mm² cross-section of a sponge sample embedded in a 36×36 mm² gelatin background. Blurred edges can be seen in the modulus image due to the bonding (connectivity) of the sponge material with the gelatin background. For composite materials that are unconnected (*i.e.*, free to slip), the presence of one material does not affect the modulus measurements in the other material; but, for connected materials, the modulus measurements are affected by the material modulus distribution in and around the vicinity of the area under the punch, resulting in poorer spatial resolution than that corresponding to the unconnected case. For such connected samples, we found the spatial resolution of the modulus images to be approximately 1.5 times the punch diameter (Srinivasan

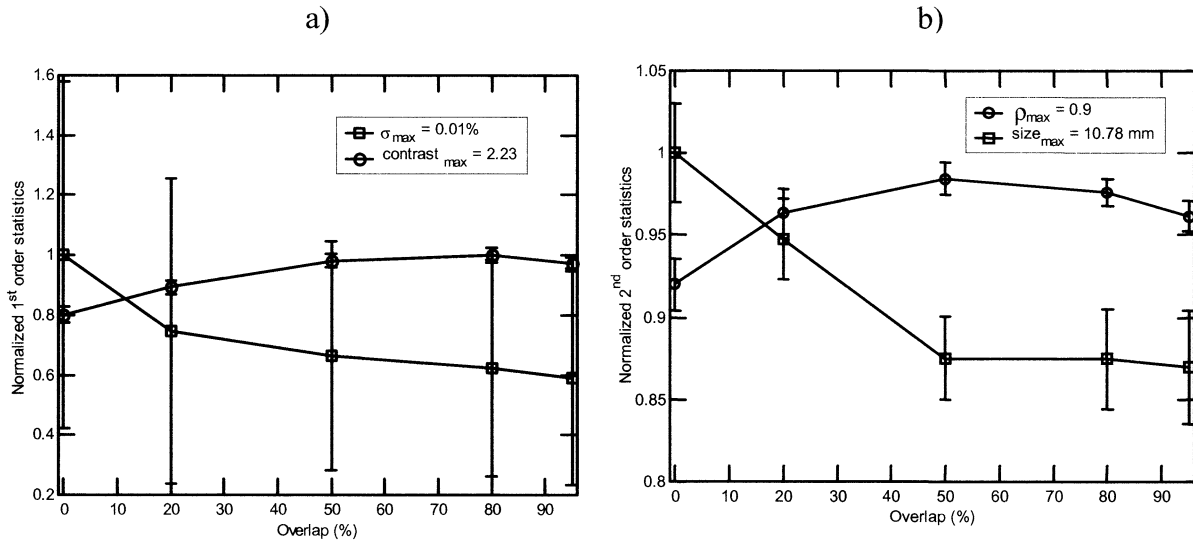


Fig. 4. (a) First order statistics and (b) second order statistics plotted as a function of the window shift for a homogeneous circular inclusion in a homogeneous background. The inclusion was 10 times stiffer than the background and a strain of 1% was applied. The simulated elastograms were computed at a window size of 2 mm.

et al. 2004). Figure 5b shows the elastogram of the same sample. The elastograms show horizontal patterns of strains, called the worm artefacts (Céspedes 1993). The optical image is also shown for comparison (Fig. 5c). Simulations and experiments were performed to study the effect of the size of the inclusion, the modulus contrast between the inclusion and the background, the applied strain and the modulus distribution within the inclusion, and the results are summarized below.

Scale. Figure 6 shows the modulus images and the elastograms at sponge sizes of 2.5 mm, 5 mm, 10 mm and 20 mm. A good correspondence between the modulus images and the elastograms can be seen for large

sample sizes. The modulus contrast and the strain contrast increase asymptotically with the size of the sponge sample, as can be observed in Fig. 6. This is due to the effect of spatial averaging because a 2-mm indenter punch was used for the modulus imaging and a 2-mm window length was used for the strain elastograms. A theoretical expression for the asymptotic improvement of contrast due to the size of the window (or the indenter punch size) relative to the target size is provided in Appendix B of Srinivasan (2003).

Figure 7 shows the first and second order statistics computed from 15 realizations. For a uniform modulus profile within the inclusion, the size of the inclusion was

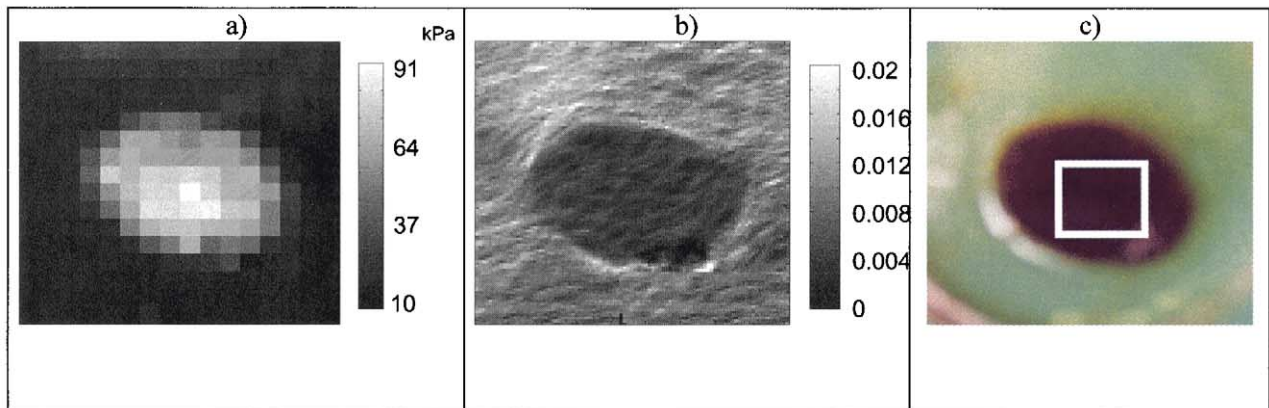


Fig. 5. (a) Modulus image at a strain of 2%, (b) strain elastogram at 1% applied strain and a precompression of 1%, and (c) photograph of a 15×20 mm² cross-section of a sponge sample embedded in a 36 mm² gelatin background.

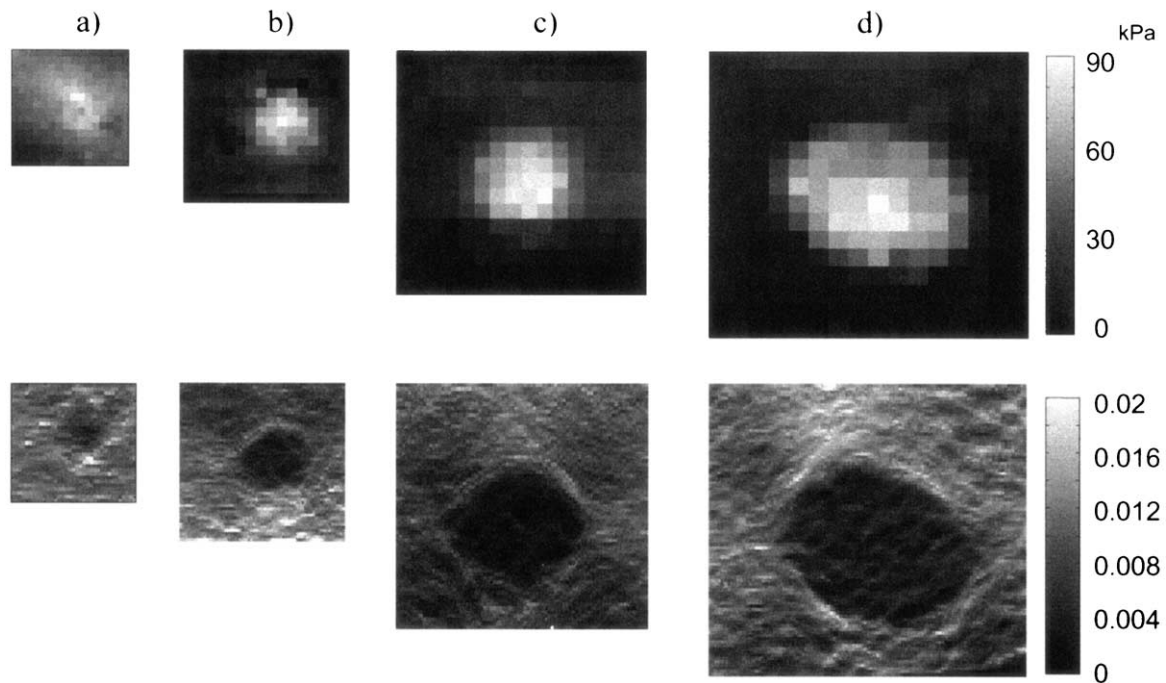


Fig. 6. Modulus image and strain elastogram of sponge samples at sizes of (a) 2.5 mm, (b) 5 mm, (c) 10 mm, and (d) 20 mm. A total of 2% strain was used to obtain the modulus images and the strain elastograms.

changed from 1 mm to 20 mm and the first and second order statistics are summarized in Fig. 7. Figure 7a shows the SD and Fig. 7b shows the modulus and strain contrast plotted as a function of the actual inclusion size. Figure 7c shows the measured inclusion sizes and Fig. 7d shows the correlation coefficient between the modulus image and the strain elastogram plotted as a function of the actual inclusion size. From Fig. 7a, it can be seen that the SD of the strain within the inclusion does not change significantly with the inclusion size in either the simulations or the experiments. The experimental phantoms also did not show statistically significant changes in the SD of the modulus measurements within the inclusion (p values > 0.05 using ANOVA). Figure 7b shows an asymptotic improvement of the strain contrast with the inclusion size in both simulations and experiments. To demonstrate an asymptotic behavior, ANOVA tests were used. The values of strain contrasts for sizes larger than 5 mm were not found to be different from each other, but were found to be significantly higher than those obtained for sizes smaller than 5 mm (p values < 0.05 using ANOVA), suggesting an asymptotic behavior. The modulus contrast in the phantom experiments increased asymptotically with the inclusion size, for reasons explained previously. The sizes in the strain images (Fig. 7c) show a very good correspondence with the size of the inclusion (*i.e.*, the size in the modulus image) and can be seen to increase linearly with the size of the inclusion. A linear regression was performed and the coefficient of de-

termination (r^2 value) was found to be more than 0.98 in both the simulations and the experiments. The value of ρ_{me} can be seen to increase asymptotically with the inclusion size in both simulations and experiments (Fig. 7d). Here too, ANOVA was used to show an asymptotic improvement of the value of ρ_{me} . The values of ρ_{me} were not found to be statistically different from one another for inclusion sizes larger than 10 mm at a 0.05 level of significance. The numerical simulations for the strain images resulted in a constant value of ρ_{me} of 0.89. The simulated elastograms resulted in a maximum value of ρ_{me} value of 0.86. The discrepancy could be attributed to digitization (Srinivasan et al. 2002a) and the presence of finite sonographic SNR (SNR_s) of 40 dB in the elastogram simulations. The phantom experiments resulted in significantly smaller values of ρ_{me} than did the simulations (maximum value of ρ_{me} value of 0.51). Some of the plausible reasons for this decrease are discussed in detail in the Discussion section.

The value of ρ_{me} as a function of the inclusion size shows two regions of operation (Fig. 7d). For inclusion sizes that were less than 10 mm (around $15 Q\lambda$), the value of ρ_{me} increased with the inclusion size. For larger inclusion sizes, the value of ρ_{me} did not improve significantly.

Contrast. The modulus images and the strain elastograms of the phantoms at several modulus contrasts are

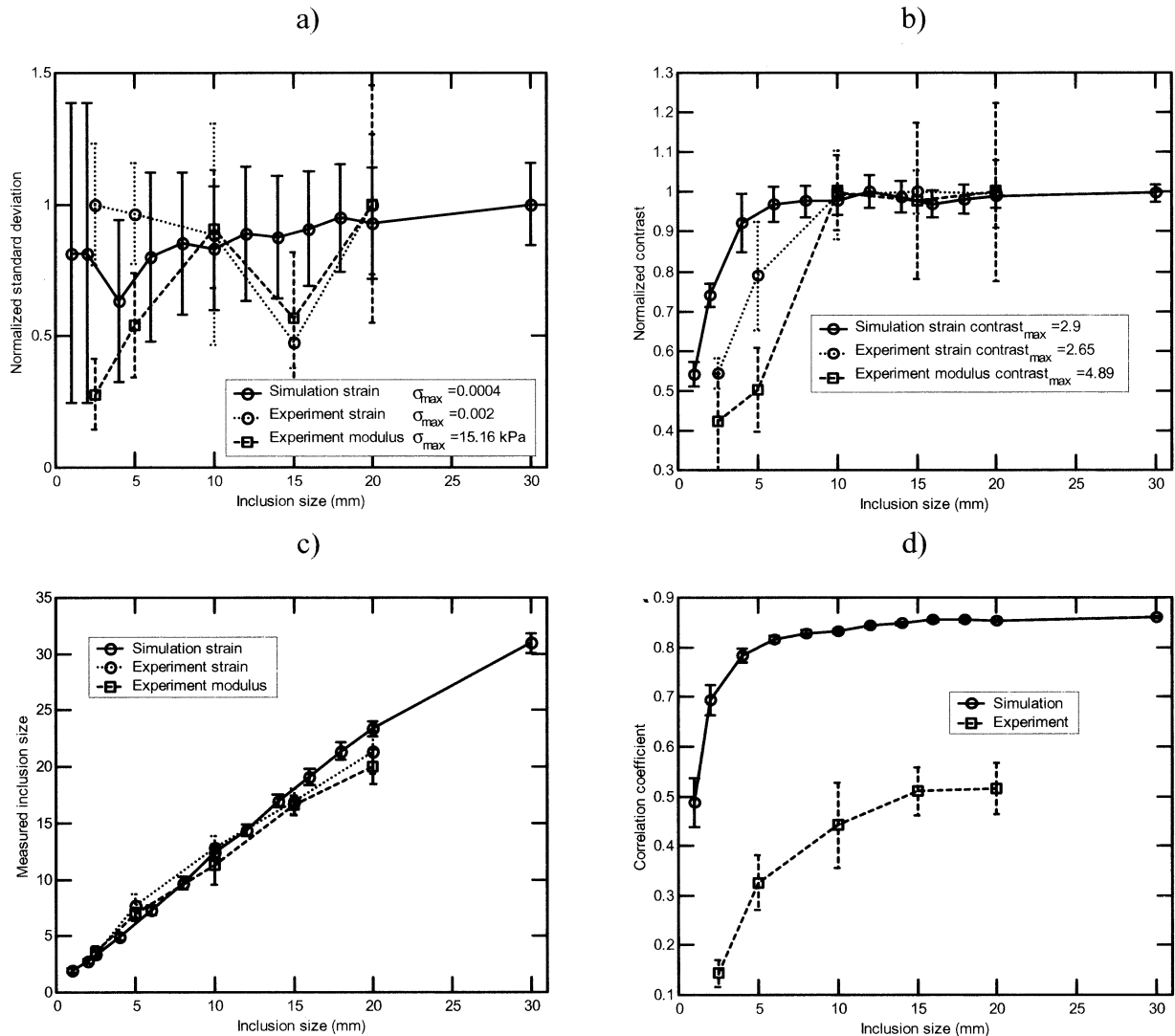


Fig. 7. (a) SD, (b) contrast, (c) size and (d) ρ_{me} plotted as a function of the size of the inclusion for the simulations and the phantom experiments. The error bars represent $\pm \sigma$ computed using 15 independent realizations for the phantom experiments and 50 realizations for the simulations. A total of 2% strain was used to obtain the modulus images and the strain elastograms.

shown in Fig. 8. The similarity between the modulus and the strain images increases with the contrast. This is due to the improvement of the contrast relative to the noise. For small contrasts, the high amount of noise (relative to the modulus or strain) in the modulus and strain images results in a poor similarity between the modulus and strain but, for high contrasts, the noise is relatively low, resulting a higher similarity.

The modulus contrast was changed from 2 to 10 and the simulation and experimental phantom results are presented in Fig. 9. The values of the SD of the strain in the inclusion were not statistically different from each other, indicating a weak dependence of the SD of the strain on the modulus contrast (Fig. 9a). The strain

contrast increased linearly with the modulus contrast, as shown in Fig. 9b. A linear regression was performed and the coefficient of determination (r^2 value) was found to be 0.99 in the simulations and 0.97 in the experiments, as expected from the contrast-transfer efficiency curves (Ponnekanti *et al.* 1995; Kallel *et al.* 1996). Note that, in Fig. 9b, a contrast-transfer efficiency of 0.5 as opposed to the true value of 1, was used for the modulus contrast of 1 (*i.e.*, the phantoms without the sponges). This was done to generate more than four points, so that the linear trend of the strain contrast curve could be clearly demonstrated. The size in the strain images does not change with the contrast, as expected (Fig. 9c). The value of ρ_{me} increases asymptotically with the contrast (Fig. 9d). The

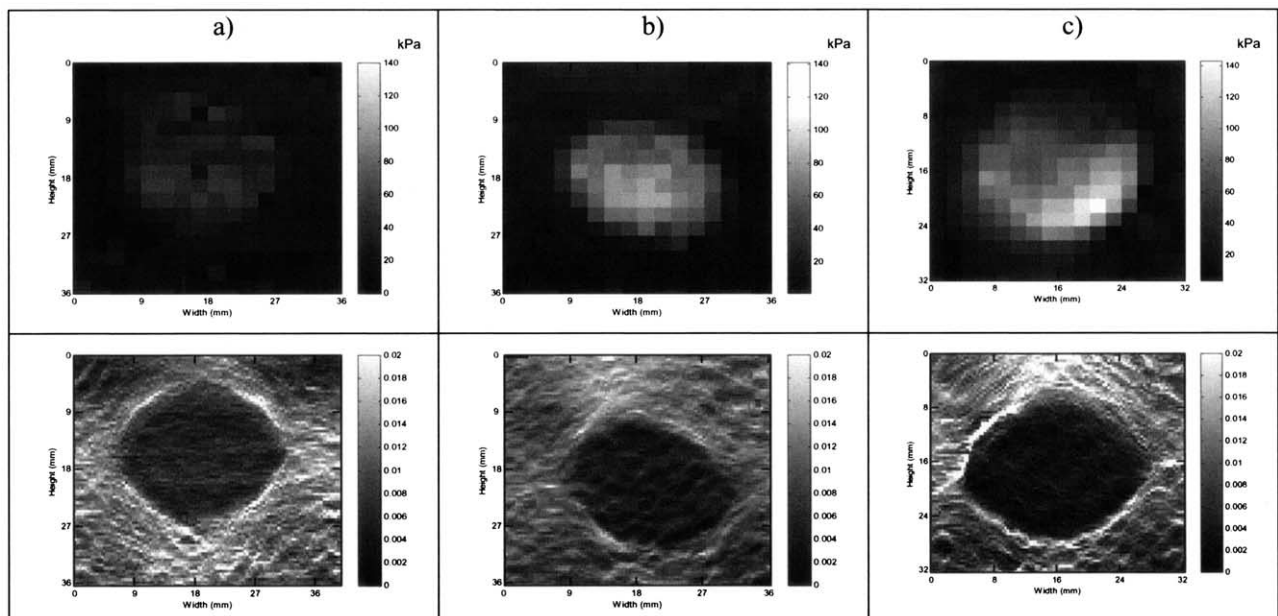


Fig. 8. (a) Modulus images and strain elastograms of sponge-reinforced gelatin samples at a modulus contrast of (a) 3, (b) 5 and (c) 6.5. A total of 2% strain was used to obtain the modulus images and the strain elastograms.

asymptotic improvement was tested as explained previously. Two regions in Fig. 9d can be identified. For contrasts smaller than 5, the value of ρ_{me} increased with the contrast. This increase is due to the improvement of the CNR with the contrast. For contrasts larger than 5, the value of ρ_{me} in the simulations remains fairly constant, that is, close to the theoretical bound of 0.89 (obtained from a correlation of the numerical modulus, inverted, and strain distributions). In the experiments, the value of ρ_{me} remains close to 0.51 for contrasts larger than 5.

Strain. Figure 10 shows a set of modulus and strain elastograms at several applied strains. The elastograms were obtained at a precompression of 1% and at applied strains varying from 0.25% to 4%. To enable a fair comparison of the modulus and strain elastograms, the modulus images were obtained at strains of 1.25% to 5%. The modulus and strain images exhibit similarities over these applied strains. Notice the decorrelation noise in the upper portion of the elastograms at a total strain of 4% (Fig. 10d). The elastogram at 0.25% applied strain (Fig. 10a) is noisy, due to the small compression used. The variation of the elastographic image quality with the applied strain is well established (Varghese and Ophir 1997).

The applied strain was changed from 0.25% to 10% and the simulation and experimental results are presented in Fig. 11. The SD of the strain increases with the applied strain (Fig. 11a), due to the increase of the decorrelation

noise with the applied strain (Varghese and Ophir 1997). The SD in the modulus shows a weak dependence on the applied strain in the measured strain range. The strain contrast in the simulations decreases with the applied strain for strains greater than 2%, due to increase in the decorrelation noise and, hence, biased measurements of strain (Fig. 11b). Figure 11c shows that the inclusion size in the strain, as well as in modulus images, is unaffected by the applied strain. However, the SD of the size measurements is high for low strains ($< 0.5\%$) as well as high strains ($> 5\%$) due to low values of SNR at high and low strains (Varghese and Ophir 1997). The value of ρ_{me} shows a convex behavior with the applied strain (Fig. 11d) in both simulations and experiments. It increases with the strain for low strains ($< 0.5\%$), due to improving SNR with the strain (Varghese and Ophir 1997). For large strains ($> 5\%$ in the simulations and greater than 3% in the experiments), the decorrelation noise in the elastograms results in a decrease of the correlation with the inverted modulus images. This behavior is similar to that of the strain filter (Varghese and Ophir 1997).

Modulus distribution. For a Gaussian modulus profile within the inclusion, the size of the inclusion was changed from 1 mm to 10 mm, the contrast of the inclusion and the applied strain were changed and the value of ρ_{me} are summarized in Fig. 12. The value of ρ_{me} appears to increase asymptotically with the inclusion size (Fig. 12a), for reasons explained earlier. The value of ρ_{me}

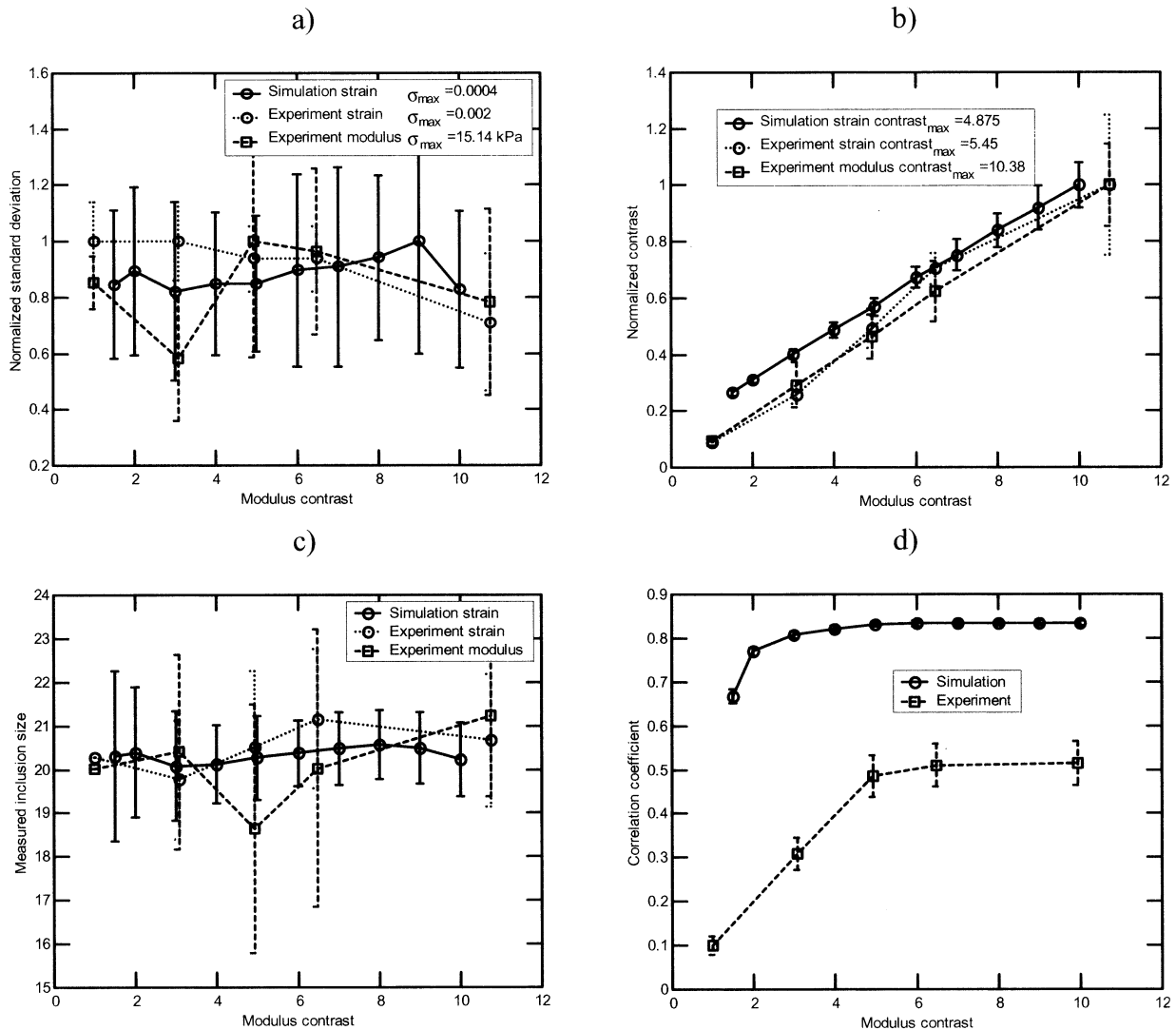


Fig. 9. (a) SD, (b) contrast, (c) size and (d) ρ_{me} plotted as a function of the modulus contrast between the inclusion and the background, for the simulations and the phantom experiments. The error bars represent $\pm \sigma$ computed using 15 independent realizations for the phantom experiments and 50 realizations for the simulations. A total of 2% strain was used to obtain the modulus images and the strain elastograms.

increases asymptotically with the contrast (Fig. 12b). The value of ρ_{me} exhibits a convex dependence on the applied strain (Fig. 12c), as explained earlier.

For a normal-random modulus distribution within the inclusion, the results are summarized in Fig. 13. The value of ρ decreases with the SD of the modulus fluctuations (Fig. 13a), but does not change with respect to the scale of the nonhomogeneities (Fig. 13b).

Due to the difficulty in replicating these modulus distributions in the phantom experiments, two types of heterogeneous phantoms were prepared. In one type, two 5-mm diameter stiff cylindrical inclusions of the same stiffness (made of sponge) were embedded inside a softer inclusion that, in turn, was embedded inside a gelatin

background. The spacing between the two stiff inclusions was varied, as shown in Fig. 14. The elastograms showed structural similarities with the modulus images, as can be seen in Fig. 14. In another type of phantom, four 10-mm diameter sponge inclusions of varying stiffness were embedded in a homogeneous gelatin background. Here too, the spacing between the inclusions was varied, as shown in Fig. 15. Structural similarities between the modulus images and the strain elastograms were observed. A statistical study was not performed here, due to difficulty in controlling the spacing between the lesions, as well as the difficulty in producing reproducible phantoms (*i.e.*, phantoms with the same arrangement of the sponges with variation of the intersample

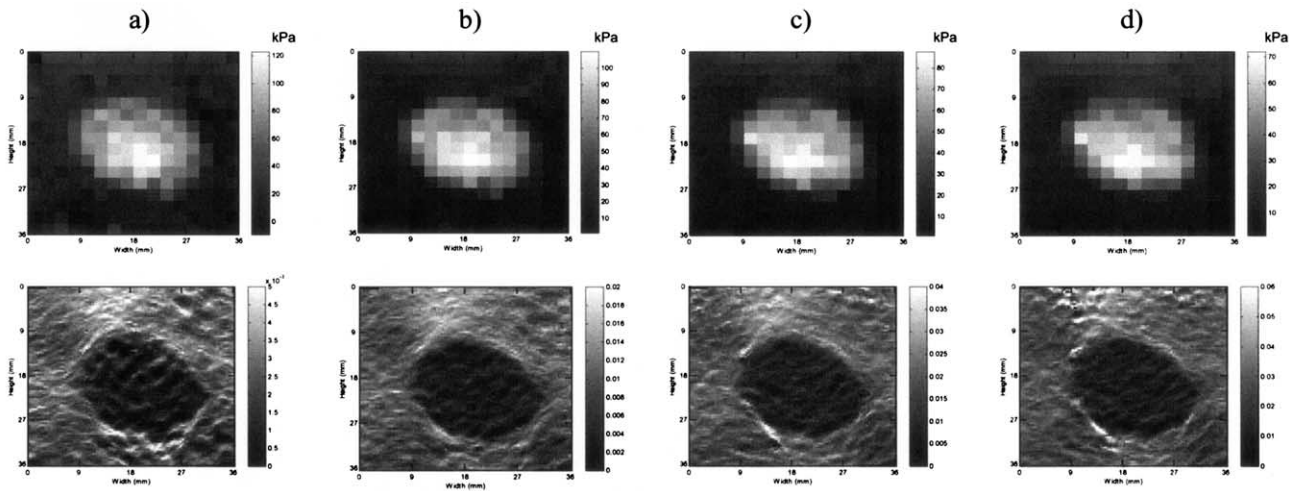


Fig. 10. Modulus images and strain elastograms of a $15 \times 20 \text{ mm}^2$ cross-section of a sponge sample embedded in a 36 mm^2 gelatin background at (a) 1.25% total strain, (b) 2% total strain, (c) 3% total strain and (d) 4% total strain.

sponge positions that are within the resolution limits of the system).

Tissue results

Beef muscle. To demonstrate a similarity of modulus and strain images for real tissue samples, thin slices (2 to 3 mm thick) of commercially available beef samples (Jordan's Foods) were imaged with the nanoindenter. Figure 16 shows the modulus image, the strain image and the picture of one of the beef slices. A good visual and structural correspondence can be seen for structures that were larger than about 3 mm. Notice the presence of decorrelation spots (high strains saturated at 4%) in the elastograms. The elastograms shown in Figure 16 were the average over five realizations. A 5×5 median filter was used in the displacement images and strain was estimated as the gradient of the displacement images. The strains of the pixels whose values of ρ (computed from the pre- and postcompression RF segments) were less than 0.7 were replaced by the strains of the neighboring pixels. Similarly, the strains of pixels outside the range of 0 to 4% were replaced by strain values of the neighboring pixels. No other spatial filtering was used on the elastograms.

The values of ρ_{me} for the beef slices computed with and without filtering are shown in Table 2. To compute the value of ρ_{me} using filtering, the strains above 4% and below 0% were replaced by the mean values of strain in the image, and a median filter of 3×3 pixels was used on the elastogram and the modulus image. Similarly, the modulus image was scaled between 10 and 100 kPa. A value of $\rho_{me} > 0.6$ can be seen between the inverted modulus and strain images with the use of filtering. The

improvement of ρ_{me} with spatial filtering can be seen in Table 2, where a $1.2 \times 1.2 \text{ mm}^2$ kernel size for the median filter (corresponding to 3×3 pixels in the elastogram) was used. The filter size was smaller than the axial resolution of the elastogram (a 2-mm window at 80% overlap was used to compute the elastogram) and, hence, the filtering was not expected to have any significant effect on the elastographic contrast or the spatial resolution. For the subsequent *ex vivo* tissue slices, the modulus image was scaled between 1 and 10 kPa and the procedure mentioned above was used for computing the elastograms as well as ρ_{me} .

Ovine kidney. Figure 17 shows a sonogram, elastogram, modulus image and optical image of an ovine kidney. The elastogram clearly represents anatomical details of the kidney, such as the medullary pyramids and the stiff cortex, as well as the outer capsule. A gross structural correspondence between the modulus image and the elastogram can be seen. The inner medulla shows up as a soft region in the modulus image (Fig. 17c) and as the high strain regions in the elastogram (Fig. 17b). The pea-shaped structures are evident from Fig. 17a and b. Similarly, the outer cortex shows up as a stiffer region in the modulus image and a low strain region in the elastogram. The capsule can also be seen in the elastogram as the outermost layer (Fig. 17b). The elastogram also shows four medullary pyramids as the high strain regions separated by low strain regions (Fig. 17b). The elastogram shown in Fig. 17 was the average over 10 elastograms. The values of ρ_{me} for the kidney slices computed with and without filtering are shown in Table 3.

Note that the values of ρ_{me} in the kidneys are lower than those obtained from the gelatin-phantom experiments. This discrepancy could be due to several reasons,

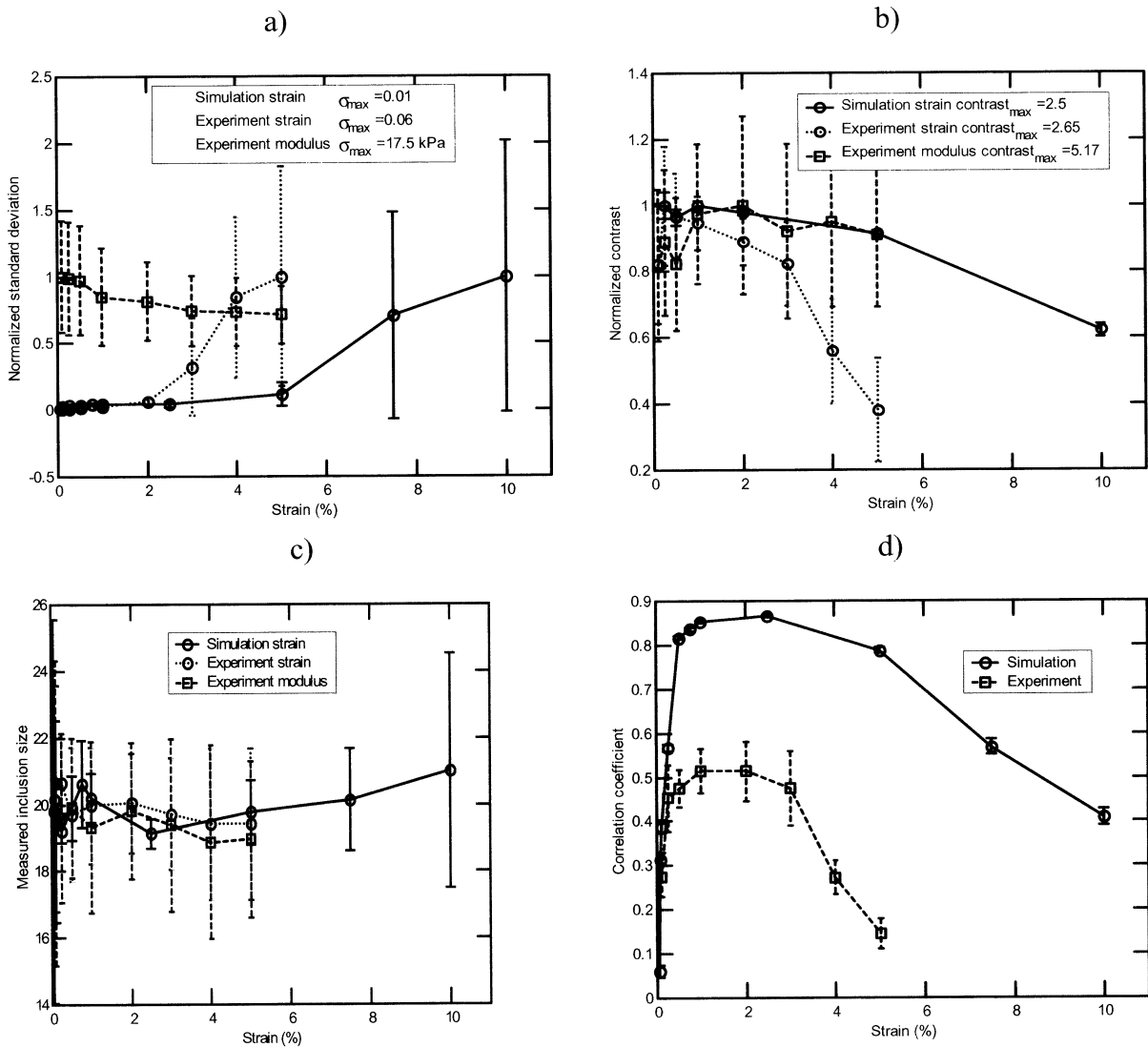


Fig. 11. (a) SD, (b) contrast, (c) size and (d) ρ_{me} plotted as a function of the applied strain for the simulations and the phantom experiments. The error bars represent $\pm \sigma$ computed using 15 independent realizations for the phantom experiments and 50 realizations for the simulations. A total of 2% strain was used to obtain the modulus images and the strain elastograms.

some of which are tissue deterioration during testing at room temperature and mechanical changes in the tissue with age, tissue relaxation and structural changes after excision from the organ, lower modulus values and, hence, relatively higher noise in the modulus images of the tissues, heterogeneity of the tissues, smaller sizes of several anatomical structures in the tissues and smaller modulus contrasts in the tissues. The modulus and strain contrasts between the anatomical regions in the kidneys were less than 2. For such low contrasts, the phantom results provided values of ρ_{me} around 0.25, which is again consistent with the results of the kidney slices.

Canine prostate. Figure 18 shows the sonograms, elastograms and modulus images obtained from three slices of a canine prostate. In the first row of Fig. 18a, the urethra shows up as a soft region (high strains) in the elastogram and the lower modulus region in the modulus image. In the second row of Fig. 18b, the two transitional zones and a central zone can be seen in the elastogram and in the modulus image. A fair visual correspondence between the structures in the modulus images and strain elastograms can be seen.

The values of ρ_{me} for the prostate slices (Fig. 18) computed with and without filtering are shown in Table 4.

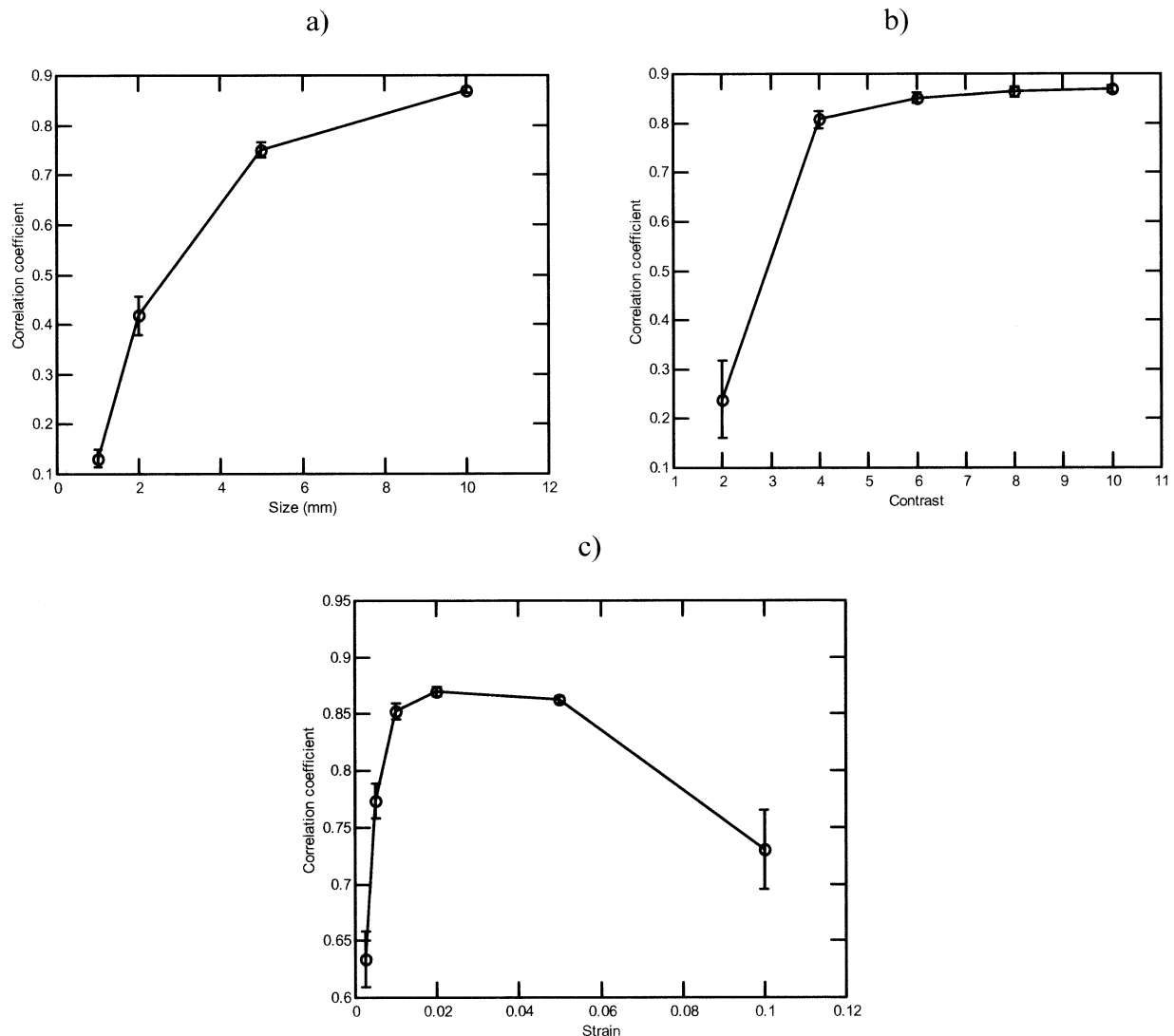


Fig. 12. Correlation coefficient plotted as a function of (a) the inclusion size for Gaussian modulus profile, (b) the size of the inclusion, and (c) the applied strain for a Gaussian modulus profile within the inclusion. An applied strain of 1% was used in the simulations.

Colon cancer. The sonograms, elastograms and modulus images of a cancer sample are shown in Fig. 19. A good visual and structural correspondence can be seen for structures seen here. The values of ρ_{me} for the cancer slices (Fig. 19) computed with and without filtering are shown in Table 5.

DISCUSSION

A comparison between the tissue modulus images and the measured strain elastograms was done to provide a meaningful interpretation of the utility of elastograms in portraying and quantifying tissue mechanical properties such as the Young's modulus. The feasibility of modulus imaging of soft tissue was first demonstrated. Prior litera-

ture studies using indentation dealt with obtaining mean modulus values of large tissue samples (more than 1 cm² cross-sectional area) and not on imaging the modulus distribution of soft tissues. The experimental results presented here indicate that nanoindentation is a useful tool for studying the local distribution of elastic moduli in soft tissue samples. A quantitative comparison between modulus images and strain elastograms was performed using simulations, phantom experiments and real tissue slices. Axial strain images were found to quantify and represent the tissue modulus distribution for cylindrical stiff targets in softer backgrounds under certain conditions, such as large sizes of targets ($> 20Q\lambda$), high modulus contrasts between the target and the background

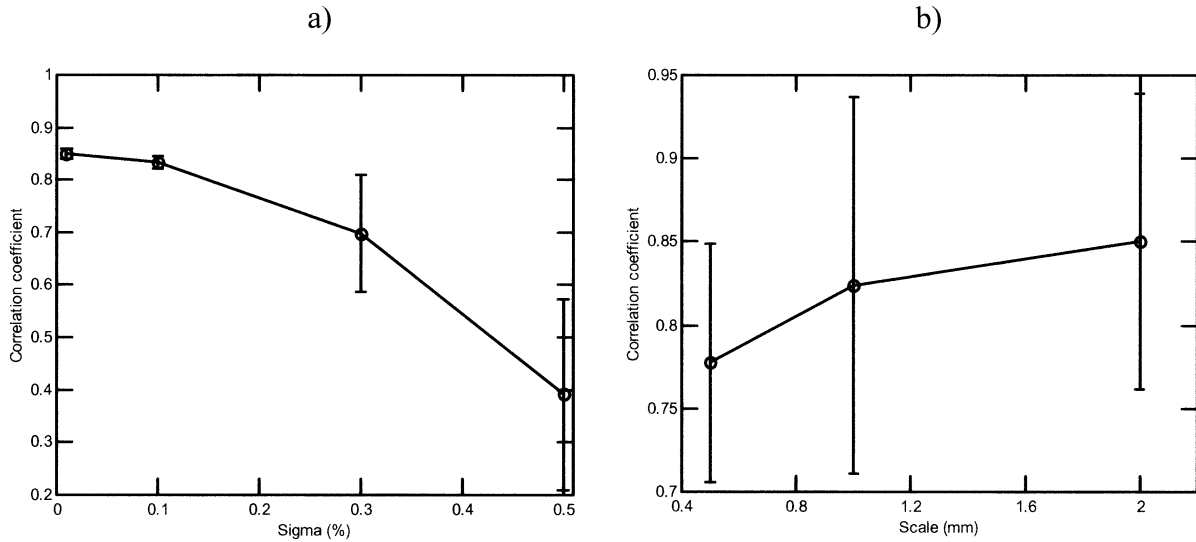


Fig. 13. Correlation coefficient plotted as a function of (a) the SD of the modulus fluctuation within the inclusion, and (b) the scale of the nonhomogeneity in the inclusion for a random modulus distribution within the inclusion. A 10-mm diameter inclusion and an applied strain of 1% were used in the simulations.

(> 5), applied strains in the range of 0.5% to 5% and external slip boundary conditions.

The correlation between the inverted modulus images and the strain images was shown progressively to

deteriorate from numerical simulations (in the absence of additive noise) to elastogram simulations (in the presence of additive noise) to experimental studies on tissue-mimicking phantoms to real tissue samples. Such a deg-

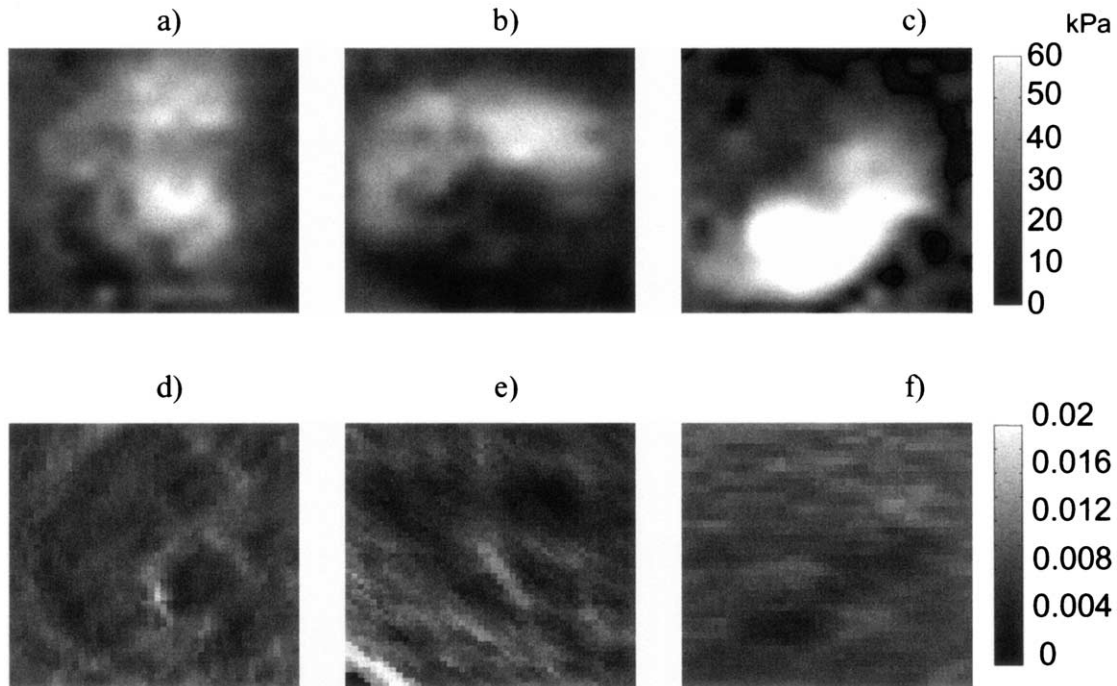


Fig. 14. Modulus images of cross-sections of two 5-mm diameter stiff cylindrical sponge inclusions embedded in a 20-mm diameter softer cylindrical sponge inclusion at several separations aligned (a) vertically, (b) horizontally, and (c) diagonally. (d), (e) and (f) Strain elastograms corresponding to the modulus images in (a), (b) and (c), respectively. A total strain of 2% was used for the modulus images and strain elastograms.

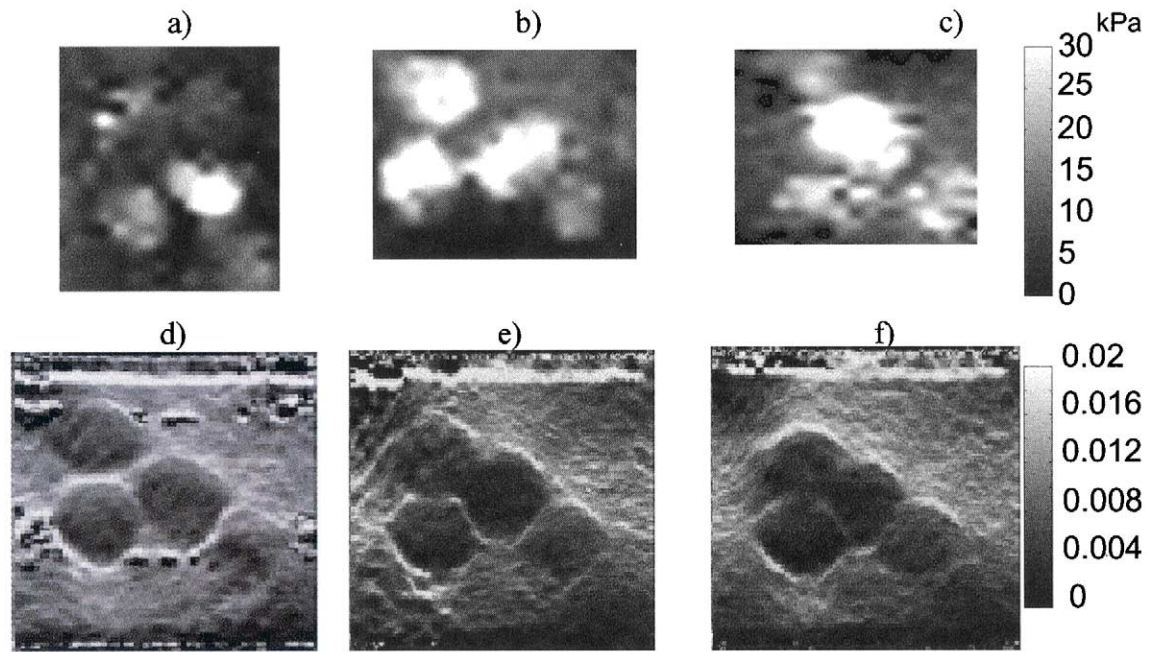


Fig. 15. (a), (b) and (c) Modulus images of cross-sections of four 10-mm diameter stiff cylindrical sponge inclusions embedded in a background at several separations. (d), (e) and (f) Strain elastograms corresponding to the modulus images in (a), (b) and (c), respectively. A total strain of 2% was used for the modulus images and strain elastograms.

radation of the results can be explained as follows. The numerical simulations assumed noise-free 2-D situations and, hence, are expected to produce the highest correlation values. Simulations of elastograms incorporated sonographic noise and also suffered from the algorithmic noise (such as digitization, the use of small window lengths, the use of interpolation and curve-fitting techniques using functional approximations) and, hence, resulted in asymptotic improvements of the modulus-strain similarities (reaching the correlation values that corresponded to the theoretical values for large values of

scales and contrasts). Phantom experiments produced smaller correspondences compared with the simulations that might be attributed to several factors, such as the three-dimensionality of the problem (the assumption of isotropy of the phantoms may be violated and out-of-plane motion could deteriorate the image quality of the elastograms), measurement noise in modulus imaging, possible violation of the assumption of sample homogeneity in the local neighborhood of the modulus measurement, deviations from the linear elasticity assumptions, nonstationary beam-related effects in the elastograms,

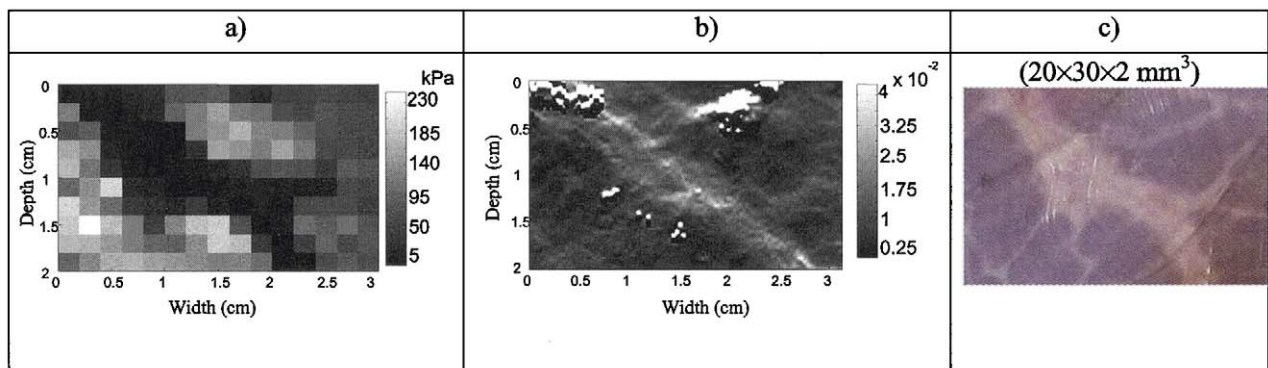


Fig. 16. (a) Modulus image, (b) strain image and (c) optical image of a beef slice. A total of 2% strain was used to obtain the modulus image and the strain elastogram.

Table 2. The values of ρ_{me} for the three beef slices

Sample	With filtering	Without filtering
1 (sample in Fig. 16)	0.71	0.58
2	0.61	0.47
3	0.68	0.49

Table 3. The values of ρ_{me} for the four ovine kidneys

Sample	With filtering	Without filtering
1 (sample in Fig. 17)	0.35	0.30
2	0.20	0.17
3	0.26	0.22
4	0.41	0.35

digitization issues in elastography and other sources of noise, such as tissue heterogeneity, that are not accounted for in the simulations. The simulation results were derated to incorporate the finite SNR and spatial resolution of modulus images in the phantom experiments. The values of the correlation coefficient were found to decrease from 0.86 to 0.76, indicating that the highest value of the correlation coefficient possible for the single-inclusion phantom model using the nanoindenter is around 0.76. The sample homogeneity and the internal boundary conditions that influence the modulus measurement at a point, were unknown and could also have contributed to the reduction of the correlation values in the phantom experiments. Yet, the correlation values were slightly more than 0.5. Experiments on real tissue slices showed further degradation of the results that might be due to the time-dependent changes in the tissues during experimentation, low SNR of the modulus images, geometrical distortions between the unexcised tissue (used in elastography) and the excised tissue (used in modulus imaging) and, also, significantly lower contrasts than those present in the simulations and phantom experiments. For example, real tissues degrade rapidly at room temperatures and the mechanical properties of tissues are known to show significant changes over time. Yet, a correlation of more than 0.25 between the modu-

lus images and strain elastograms was observed consistently over several tissue types, such as kidneys, prostates, cancers and beef slices. Low correlation values of around 0.3 were observed at modulus contrasts of 2 and were consistent with the results of the phantom experiments. Tissue structures such as beef slices and certain cancers showed modulus contrasts of more than 5. For such structures, the correlation values were around 0.5 and that was, again, consistent with the results of the phantom experiments.

The correlation between the inverted modulus images and strain elastograms can be expressed in terms of imaging parameters such as the CNR, the axial resolution and the dynamic range of strains. The CNR is a parameter that is affected by the scale of the problem (*i.e.*, the target size), as well as the noise properties of the elastograms. For example, for target sizes that are smaller than the window length used for strain estimation, a loss of strain contrast is expected to occur. Therefore, for such a case, the CNR as well as the value of ρ_{me} are expected to be small. For target sizes that are larger than the window length, the SNR and CNR improve with the window length, resulting in improvements in the values of ρ_{me} . For small window lengths that are comparable with the axial resolution, the high noise in the elasto-

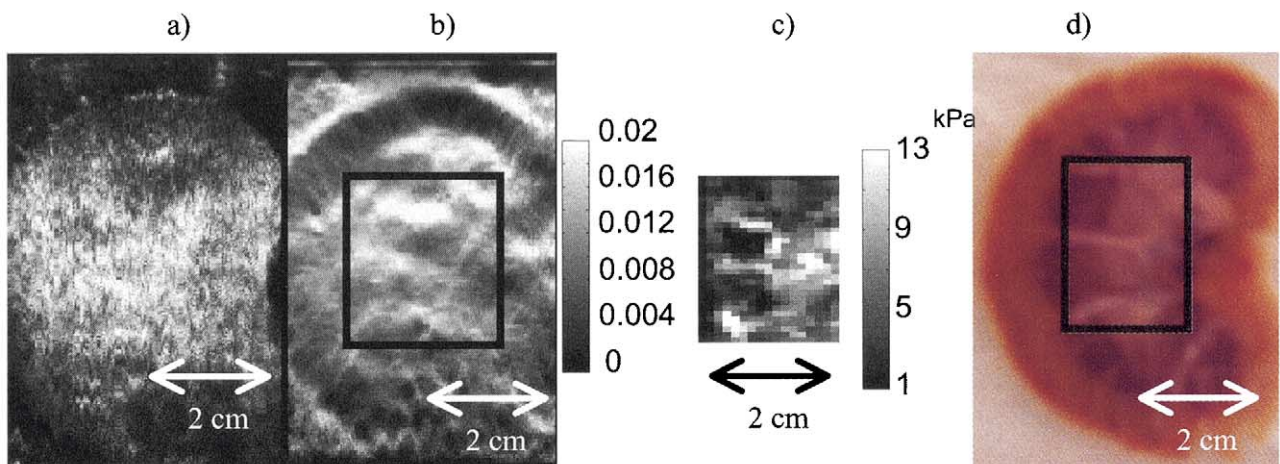


Fig. 17. (a) Sonogram, (b) elastogram, (c) modulus image and (d) optical image of an ovine kidney. A total of 2% strain was used to obtain the modulus image and the strain elastogram.

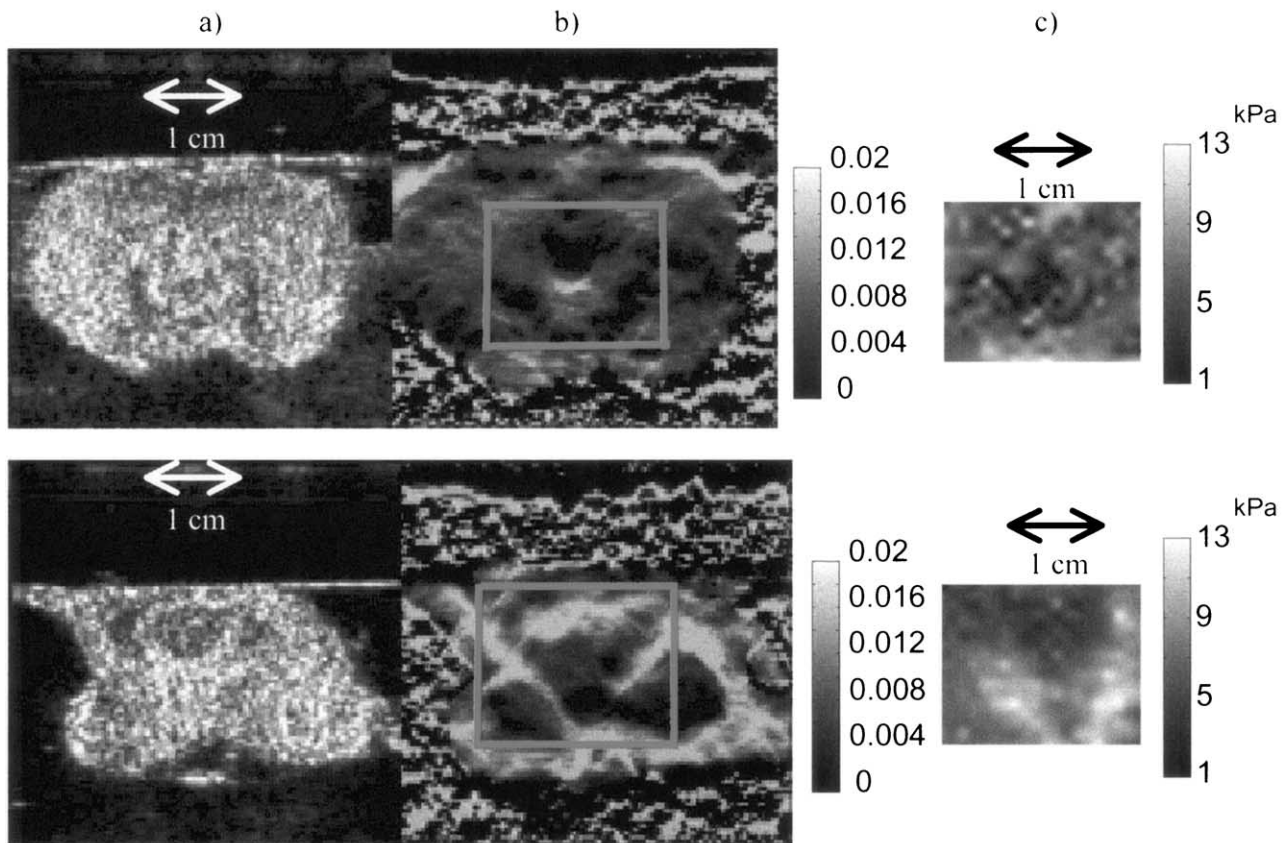


Fig. 18. (a) Sonograms, (b) elastograms and (c) modulus images at two planes of a canine prostate. A total of 2% strain was used to obtain the modulus images and the strain elastograms.

grams results in low values of CNR as well as low values of ρ_{me} . Therefore, maximizing the CNR would also maximize the value of ρ_{me} . The simulations presented earlier supported this observation.

Srinivasan et al. (2003) showed that the spatial resolution (axial as well as lateral) of the axial strain elastograms was equal to the window length in the axial direction and the beam width in the lateral direction. The SNR and CNR were also shown to improve at a more than a linear rate with the window length, indicating an improvement of the modulus-strain correlation with the window length, and the axial resolution of the image

deteriorates linearly with the window length (Varghese and Ophir 1997; Srinivasan et al. 2003). This indicates an inverse relationship between the axial resolution and the value of ρ_{me} . However, when the axial resolution (*i.e.*, the window length) is larger than the target size, the loss of axial resolution is also accompanied by a loss of contrast (*i.e.*, nonresolvable scales) and, hence, a reduction of the CNR and the correlation between the modulus and the strain elastograms. Therefore, the value of ρ_{me} is expected to show a convex behavior with the axial resolution for elastographically resolvable scales.

Although cross-correlation is used widely as a statistic in method-comparison studies, the use of cross-correlation alone is not sufficient to indicate the similarities between modulus and strain images. This is because the correlation coefficient is a gross indicator of structural similarities and it depends on other image quality factors, such as SNR, CNR and spatial resolution. A trade-off between these quality factors affects the correlation coefficient, as well. For example, spatial filtering improves the image SNR, typically at the expense of image contrast and spatial resolution. Yet, the correlation

Table 4. The values of ρ_{me} for two canine prostates

Sample	With filtering	Without filtering
1 - plane 1 (first row of Fig. 18)	0.33	0.30
1 - plane 2 (second row of Fig. 18)	0.48	0.44
1 - plane 3	0.37	0.33
2 - plane 1	0.32	0.29
2 - plane 2	0.35	0.32
2 - plane 3	0.28	0.25

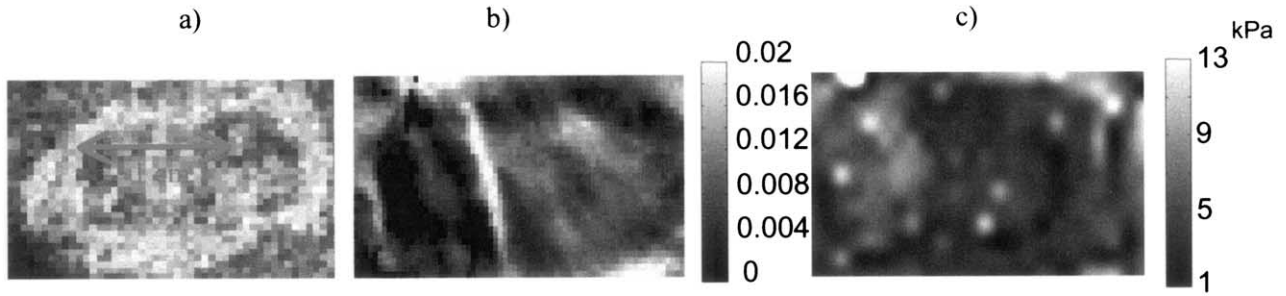


Fig. 19. (a) Sonogram, (b) elastogram and (c) modulus image of a colon cancer. A total of 2% strain was used to obtain the modulus image and the strain elastogram.

coefficient improves with the image SNR as long as the deteriorations of contrast and resolution are not severe. The improvement of the correlation coefficient with the filter size is likely to show a convex-shaped curve, with the highest value occurring at values of SNR, CNR and resolution that are intermediate between low and high values.

This study focused on comparing modulus images with strain elastograms for several parameters, such as the modulus contrast, the scale of the targets, the modulus distribution and the applied strain. Other controlling factors on the modulus-strain comparison, such as the boundary conditions and the connectivity of the tissue elements, were not studied. The boundary conditions influence the uniformity of the stress field in elastography and, hence, the modulus-strain correspondence. We used a compressor with a cross-sectional dimension that was larger than the sample dimensions, to reduce the stress decay. Ensuring perfect slip boundary conditions at the compressor, as well as at the base, was not feasible. Hence, a small degree of strain decay was present, which could have affected the correspondence between modulus and strain to a small degree. A systematic study of the role of the boundary conditions on the modulus-strain correspondence is beyond the scope of this work.

CONCLUSION

An important conclusion of this work is that axial strain elastograms are correlated to the inverted modulus images for several anatomical structures, such as stiff

tumors in a homogeneous background, the kidney, the prostate, colon cancers and even for anisotropic materials such as beef muscle. A quantitative comparison between modulus images and strain elastograms using simulations and phantom experiments showed high values of correlation at elastographically resolvable scales. Axial strain images were found to quantify and represent the tissue modulus distribution for cylindrical stiff targets in softer backgrounds under certain conditions such as large sizes of targets ($> 20Q\lambda$), high modulus contrasts between the target and the background (> 5), applied strains in the range of 0.5% to 5% and slippery external boundary conditions.

Similarities between the modulus images and strain images were quantified using first order statistics, such as contrast and SD, and second order statistics, such as the correlation coefficient and size. A good correspondence between the modulus and strain images was obtained at several resolvable scales, modulus contrasts and applied strains. Theoretical models of a stiff cylindrical inclusion inside a soft homogeneous background resulted in correlation values of around 0.9 between the inverted modulus image and the strain image. Simulation models resulted in a range of correlation values that increased asymptotically to a value of 0.86. Phantom models mentioned above resulted in correlation values that increased asymptotically to a value of 0.5. Experiments in real tissue, such as colon cancers, kidneys, prostates and beef slices, resulted in average correlation values from 0.3 to 0.5. An asymptotic improvement of the correlation between the inverted modulus image and strain image was found with respect to factors such as the modulus contrast and scale. A convex dependence between the correlation coefficient and factors such as the applied strain and the window length, was found.

With reduction of experimental noise, improvement of the elastographic and modulus imaging parameters and adequate control of the experimental conditions, the correlation between the inverted modulus image and

Table 5. The values of ρ_{me} for four colon cancer slices

Sample	With filtering	Without filtering
1 (in Fig. 19)	0.35	0.30
2	0.31	0.25
3	0.41	0.36
4	0.28	0.24

strain elastograms of soft tissues may be improved from the values of 0.3 upward toward those that are predicted by the simulations. The experimental results indicated that it is feasible to obtain quantitative modulus information from nanoindentation of soft tissues, as well as to perform a quantitative comparison between modulus images and strain images under certain conditions.

REFERENCES

- Alam SK, Ophir J, Konofagou E. An adaptive strain estimator for elastography. *IEEE Trans Ultrason Ferroelec Freq Control* 1998; 45(2):461–472.
- Anderson PM, Glaser E, Veress A, et al. Using indentation and intravascular ultrasound to measure arterial response. In: West JL, Nerem R, Goupil D, eds. *Material Research Society Symposium Proceedings 662 on Cardiovascular biomaterials*, 2001. Warrendale, PA: Materials Research Society, 2001:MM2 .4.
- Binnig G, Quate CF, Gerber CH. Atomic force microscope. *Phys Rev Lett* 1986;56(9):930–933.
- Céspedes I. *Elastography: Imaging of biological tissue elasticity*. Ph.D. dissertation, University of Houston, 1993.
- Chen EJ, Novakofski J, Jenkins WK, O'Brien WD Jr. Young's modulus measurements of soft tissues with application to elasticity imaging. *IEEE Trans Ultrason Ferroelec Freq Control* 1996;43: 191–194.
- Doyley MM. An investigation into methods for improving the clinical usefulness of elasticity imaging. Ph.D. dissertation, University of London, 1999.
- Duck FA. *Physical properties of tissue*. San Diego, CA: Academic Press, 1990.
- Emelianov SY, Lubinski MA, Weitzel WF, et al. Elasticity imaging for early detection of renal pathology. *Ultrasound Med. Biol* 1995;21: 871–883.
- Fung YC. *Biomechanics: Mechanical properties of living tissues*, 2nd ed. New York: Springer-Verlag, 1993.
- Gao L, Parker KJ, Lerner RM, Levinson SF. Imaging of the elastic properties of tissue—A review. *Ultrasound Med Biol* 1996;22:959–977.
- Garra BS, Céspedes EI, Ophir J, et al. Elastography of breast lesions: Initial clinical results. *Radiology* 1997;202:79–86.
- Hall JT, Zhu Y, Spalding CS. In vivo real-time freehand palpation imaging. *Ultrasound Med Biol* 2003;29(3):427–435.
- Hiltawsky KK, Kruger M, Starke C, et al. Freehand ultrasound elastography of breast lesions: Clinical results. *Ultrasound Med Biol* 2001;27(11):1461–1469.
- Howe RD. Remote palpation technology. *IEEE Eng Med Biol* 1995; 14(3):318–323.
- Kallel F, Bertrand M. Tissue elasticity reconstruction using linear perturbation method. *IEEE Trans Med Imaging* 1996;15(3):299–313.
- Kallel F, Bertrand M, Ophir J. Fundamental limitations on the contrast-transfer efficiency in elastography: An analytic study. *Ultrasound Med Biol* 1996;22(4):463–470.
- Kallel F, Ophir J, Magee K, Krouskop T. Elastographic imaging of low-contrast elastic modulus distributions in tissue. *Ultrasound Med Biol* 1998;24(3):409–425.
- Kallel F, Prihoda CD, Ophir J. Contrast-transfer efficiency for continuously varying tissue moduli: Simulation and phantom validation. *Ultrasound Med Biol* 2001;27(8):1115–1125.
- Konofagou EE, D'Hooge J, Ophir J. Myocardial elastography—A feasibility study *in vivo*. *Ultrasound Med Biol* 2002;28(4):475–482.
- Krouskop TA, Wheeler TM, Kallel F, Hall T. The elastic moduli of breast and prostate tissues under compression. *Ultrasound Imaging* 1998;20:151–159.
- Lorenz A, Sommerfeld HJ, Schurmann MG, et al. A new system for the acquisition of ultrasonic multicompression strain images of the human prostate *in vivo*. *IEEE Trans Ultrason Ferroelec Freq Control* 1999;46(5):1147–1154.
- Nightingale K, Soo MS, Trahey G. Acoustic radiation force impulse imaging: *In vivo* demonstration of clinical feasibility. *Ultrasound Med Biol* 2002;28(2):227–235.
- Oliver WC, Pharr GM. An improved technique for determining hardness and elastic modulus using load and displacement sensing indentation experiments. *J Mat Res* 1992;7:1564–1583.
- Ophir J, Alam SK, Garra B, et al. Elastography: Ultrasonic estimation and imaging of the elastic properties of tissues. *Proceedings of the Institute of Mechanical Engineering Part H. Eng Med* 1999;213: 203–233.
- Ophir J, Céspedes I, Ponnekanti H, Yazdi Y, Li X. Elastography: A quantitative method for imaging the elasticity of biological tissues. *Ultrasound Imaging* 1991;13:111–134.
- Pesavento A, Perry C, Krueger M, Emert H. A time efficient, and accurate strain estimation concept for ultrasonic elastography using iterative phase zero estimation. *IEEE Trans Ultrason Ferroelec Freq Control* 1999;46:1057–1067.
- Ponnekanti H, Ophir J, Huang Y, Céspedes I. Fundamental mechanical limitations on the visualization of elasticity contrast in elastography. *Ultrasound Med Biol* 1995;21:533–543.
- Rho JY, Zioupos P, Currey JD, Pharr GM. Microstructural elasticity and regional heterogeneity in human femoral bone of various ages examined by nanoindentation. *J Biomech* 2002;35:189–198.
- Righetti R, Kallel F, Stafford RJ, et al. Elastographic characterization of HIFU-induced lesions in canine livers. *Ultrasound Med Biol* 1999;25(7):1099–1113.
- Sarvazyan AP. Mechanical imaging: A new technology for medical diagnostics. *Int J Med Inf* 1998;49:195–216.
- Sarvazyan AP, Skovoroda AR, Emelianov SY, et al. Biophysical bases of elasticity imaging. In: Jones P, ed. *Acoustical imaging*. New York: Plenum Press, 1995:21.
- Skovoroda A, Emelianov S, O'Donnell M. Tissue elasticity reconstruction based on ultrasonic displacement and strain images. *IEEE Trans Ultrason Ferroelec Freq Control* 1995;42:747–765.
- Souchon R, Rouvière O, Gelet A, et al. Visualization of HIFU lesions using elastography of the prostate *in vivo*: Preliminary results. *Ultrasound Med Biol* 2003;29(7):1007–1015.
- Srinivasan S. Comparing elastographic strain images with modulus images obtained using a nano-indenter: Applications in characterizing the mechanical properties of tissues. Ph.D. dissertation, University of Houston, 2003.
- Srinivasan S, Kallel F, Ophir J. The effects of digitization on the elastographic signal-to-noise ratio. *Ultrasound Med Biol* 2002a; 28(11):1521–1534.
- Srinivasan S, Kallel F, Souchon R, Ophir J. Analysis of an adaptive strain estimation technique in elastography. *Ultrasound Imaging* 2002b;24:109–118.
- Srinivasan S, Krouskop T, Ophir J. Comparing elastographic strain images with modulus images obtained using nanoindentation: Preliminary results using phantoms and tissue samples. *Ultrasound Med Biol* 2004;30(3):329–344.
- Srinivasan S, Righetti R, Ophir J. Trade-offs between axial resolution and signal-to-noise ratio in elastography. *Ultrasound Med Biol* 2003;29(6):847–866.
- Sumi C, Suzuki A, Nakayama K. Estimation of shear modulus distribution in soft tissues from soft tissue distribution. *IEEE Trans Biomed Eng* 1995;42:193–202.
- Trahey GE, Nightingale K, Nightingale R, Bentley R. ARFI imaging of ex-vivo and in-vivo human tissues. In: Linzer M, ed. *27th International Symposium on Ultrasonic Imaging and Tissue Characterization*, Arlington VA. *Ultrasound Imaging*, 2002, 22:176.
- Varghese T, Ophir J. A theoretical framework for performance characterization of elastography: The strain filter. *IEEE Trans Ultrason Ferroelec Freq Control* 1997;44(1):164–172.
- Varghese T, Zagzebski JA, Techavipoo U, et al. Elastographic imaging of thermal lesions *in vivo*. In: Linzer M, ed. *27th International Symposium on Ultrasonic Imaging and Tissue Characterization*, Arlington VA. *Ultrasound Imaging*, 2002, 22:175.
- Wellman PW, Howe RD. Modeling probe and tissue interaction for tumor feature extraction. *ASME Summer Bioengineering Conference*, Sun River, OR, June 1997. *ASME* 1997;35:237–238.